ZDR - Simulation Studies of the NLC Main Linacs*

R. Assmann, C. Adolphsen, K. Bane,
K. Thompson, T. O. Raubenheimer

Stanford Linear Accelerator Center, Stanford, California 94309

May 1996

Abstract

This study was published as part of the Next Linear Collider (NLC) Zeroth order Design Report (ZDR) [1]. It addresses the problems of transporting very small emittance beams in the main linacs of the NLC. Several mechanisms of emittance dilution and correction are calculated in detail. The results demonstrate the feasibility of the NLC main linac design under the assumption that the specified device tolerances are met. The full text of the ZDR is available on the WWW under "http://www.slac.stanford.edu/accel/nlc/zdr/".

1 Introduction

The previous sections of the ZDR describe the basic design of the NLC main linacs. The results of analytical estimates and numerical simulations were used throughout the text, mainly to discuss and justify specific design choices. In this section, we describe numerical calculations that were performed to study the NLC main linacs in greater detail. By assuming realistic errors in all major accelerator components, we can study the complex interactions between different mechanisms of emittance growth and the proposed correction algorithms. Since stability problems are of major concern for the NLC, we also discuss simulation results for the alignment stability in the NLC main linacs.

In the following, we will briefly describe the simulation program LIAR ("LInear Accelerator Research code") which was recently developed. Then, we discuss the overall objectives for the NLC linac simulations and present the simulation results. A final outlook will present the conclusions and will describe directions for future work.

The goal of the simulation studies done so far is to show the feasibility of the acceleration and emittance preservation in the NLC linacs. Several important problems still do not have their final solutions. However, we will show that we have working solutions to the major problems that already fulfil the requirements.

*Work supported by the Department of Energy, contract DE-AC03-76SF00515

2 Simulation program

The simulation and tracking program LIAR ("LInear Accelerator Research code") is designed as a general tool to study the beam dynamics of linacs. LIAR's major design goals are to provide a simulation platform that includes all the basic accelerator physics for linacs, that allows to add easily advanced features and that is not bound to a specific linac design. Presently LIAR is used both for NLC and SLC simulations. We briefly describe its main features and observables.

All magnets are simulated using the thick lens representation. The beamline description includes "realistic" support points with a number of elements mounted on a common girder. Thus we can simulate the effects of ground motion and we can also study correction algorithms using movers at the support points. RF structures can be divided into pieces and have an RF-BPM assigned at both ends.

The beam is described as a train of bunches. Each bunch is divided into slices along the longitudinal direction and each slice is described by a number of mono-energetic beam ellipses. The tracking part of the program performs a 6D coupled beam transport including the beam-induced transverse and longitudinal wakefields in the RF structures.

The basic features of the simulation program are complemented by the ability to set random and systematic errors on most accelerator parameters:

1. Transverse misalignments and roll angles for most element types.
2. BPM misalignments with respect to the quadrupoles. Finite BPM resolution.
3. Strength errors for quadrupoles, bending magnets and correctors.
4. Phase and gradient errors of the RF structures.
5. Random or "ATL"-like misalignments of the accelerator support.
6. Misalignments of individual RF structure pieces ("bowing", etc.).

Given those capabilities we can simulate basic and advanced optimization schemes for the main linacs of NLC. So far the following correction methods have been implemented:

1. One-to-one steering using dipole correctors.
2. Trajectory feedbacks.
3. Beam-based quadrupole alignment.
4. Beam-based alignment of the RF structures.
5. SLC type emittance bumps with deterministic optimization.

Other optimization schemes like dispersion-free steering or multibunch kickers will be added in the future. All those correction schemes can be applied and tested in the presence of multiple interacting error sources. Furthermore we can study the convergence of these techniques when they are iterated many times.

We use a number of different measures to describe the performance of the linacs. Many observables are available at each BPM so that they can easily be studied as a function of longitudinal position s:

1. Horizontal and vertical beam and bunch positions with respect to the design plane or the BPM centers (by beam we refer to the average of the bunches).
2. Horizontal and vertical emittances for all bunches.
3. Horizontal and vertical luminosity reduction for all bunches.
4. Energy spread of the beam.
5. Beam energy.
6. Horizontal and vertical BMAG (see Equation 8.3) for a selected bunch.

At every marker point the beam distribution in phase space is available for a selected bunch and the whole bunch train. Twiss parameters are available for every beamline element. All observables, together with other parameters like misalignments, can be saved into external files which then are further analyzed. LIAR also provides screen summary output about single and multibunch emittance growth, rms trajectory offsets and the other observables.

3 Objectives

The NLC main linac simulations are undertaken with the general objectives to study the complex interactions between different parameters and to get a complete and coherent picture of the relevant emittance growth and optimization processes. By studying multiple error sources we try to evaluate the main linac performance under "realistic" conditions. Here we give a list of relevant simulation studies.

- Static quadrupole and BPM misalignments and errors (compare Sections 8.3.4 and 8.3.6):
  - Dispersive emittance growth as a function of transverse quadrupole and BPM misalignments.
  - Sensitivity to lattice mismatch from quadrupole strength errors.
  - Sensitivity to betatron coupling from quadrupole rolls.
- Static structure misalignments and errors (compare Sections 8.3.4 and 8.3.6):

  - Emittance growth due to random structure misalignments. Sensitivity to different wavelengths of misalignments.
  - Emittance growth due to systematic structure misalignments ("bowing", etc.).
  - Lattice mismatch from gradient and phase errors.
  - Sensitivity of dispersive emittance growth to changes in the BNS phases.

- Beam tails:
  - Determination of the average beam power that needs to be collimated.

- Beamline stability (compare Section 8.4):
  - Emittance growth from ATL-like drifts of the quadrupole and structure alignment.
  - Emittance growth from jitter and vibrations of the accelerator support.
  - Feedback requirements for effective trajectory stablization.
  - Effects from bunch-to-bunch variations of charge or initial position and angle.

- Emittance control techniques (compare Section 8.4.2):
  - Efficiency of interleaved quadrupole steering and RF structure alignment in the presence of errors (compare Section 8.4.2).
  - Dispersion-free and wakefield-free steering.
  - Emittance optimization with trajectory bumps.

Several of these studies are interdependent and some need to be done for both single-bunch and multibunch cases. We cannot yet present all the final results. However, most of the problems mentioned above are addressed in the simulations that we are going to present.

4 Simulation parameters

The NLC tolerances are tighter for the higher bunch currents and the longer bunch lengths at the higher beam energies. Therefore we restrict the simulations to the 500 GeV version of NLC-II. This is the case "NLC-IIb" in Tables 8-1 and 8-2. The beam consists of 90 bunches, where each bunch contains 1.1×10^{10} particles, is 150 μm long and has an initial uncorrelated energy spread of 1.5%. We describe a single bunch at 10 longitudinal positions with each 3 monoenergetic beam slices. The initial bunch shape is Gaussian. The initial horizontal and vertical beam emittances are $\gamma\epsilon_x = 4.0 \times 10^{-6}$m-rad and $\gamma\epsilon_y = 4.0 \times 10^{-8}$m-rad. The beam is accelerated to a final beam energy of 500 GeV.

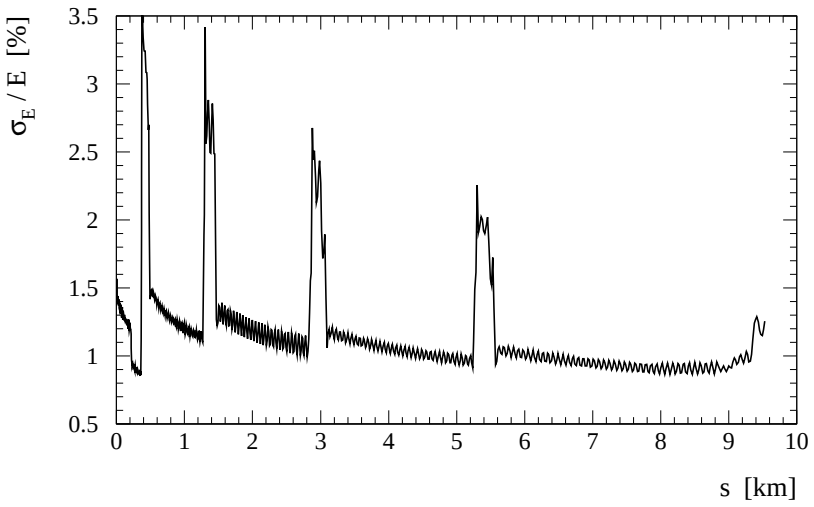

Figure 1: A simple 2-particle model (compare Equation 8.2) yields the correlated energy spread that is required for autophasing. If the large values for the diagnostics stations are ignored the simple model predicts that an average correlated energy spread of about 1.1% is needed for autophasing.

The full NLC-IIb lattice is used for the simulations and we assume that the chicanes in the diagnostics stations are switched off. Beyond that we assume that multibunch beam loading is perfectly compensated. Parametrizations for short-range and long-range wakefields were provided from detailed calculations as mentioned in Sections 8.3.1 and 8.3.2. The simulations that are presented here focus on the vertical plane where the small initial emittance makes it much harder to avoid dilutions.

5 BNS configuration

As explained in Section 8.2.2 BNS damping significantly reduces the emittance growth in a linac. If the BNS autophasing condition is fulfilled then an incoming betatron oscillation will propagate downstream without perturbation. In this case, there will be minimal emittance growth. Figure 1 shows the autophasing energy spread for a simple two particle model (compare Equation 8.2). The figure suggests an average autophasing energy spread of about 1.1%.

In order to identify an optimal BNS configuration we studied a number of energy spread profiles along the linac, each of which is generated by adjusting the RF phases in three groups. The BNS configurations number 1 to 9 are defined in Table 5. All BNS cases were calculated to give the required final beam energy spread of about 0.3% rms. In Figure 2 we show the beam energy spread along the linac for the different cases. Figure 3

Config	ϕ_1 [°]	E_1 [GeV]	ϕ_2 [°]	E_2 [GeV]	ϕ_3 [°]
1	4	30	-7	485	-30
2	8	30	-5	455	-30
3	10	30	-3	425	-30
4	12	30	-1	400	-30
5	14	30	1	380	-30
6	16	30	3	360	-30
7	18	30	5	335	-30
8	20	30	7	320	-30
9	22	30	9	300	-30

Table 1: BNS configurations: ϕ_1, ϕ_2 and ϕ_3 are the three RF phases in the linac and E_1 and E_2 are the switching points.

characterizes the different BNS configurations in terms of average energy spread and the energy overhead required to generate them. The energy overhead is defined as the energy difference between operating with the nominal average RF phase and operating with the BNS phases. In the following we refer to the BNS cases by their BNS energy overhead.

To study the BNS configurations in terms of emittance preservation, we simulated the emittance growth for an initial 1σ vertical beam offset (2.2 μm). The initial uncorrelated beam energy spread was set to zero. As is shown in Figure 3 we find the smallest emittance growth for a BNS energy overhead of 1.3%. For lower energy overheads wakefields cause large emittance growth while dispersive emittance growth dominates for higher BNS energy spreads. Since the BNS overhead of 1.3% is well inside the specifications (up to 3%), we chose the BNS configuration number 3 for all further studies. However, we always made sure that this BNS case is a good working point. Later we will discuss our choice of BNS energy spread for two other emittance growth problems and we will see that the BNS configuration number 3 is still the optimal working point within the cases that are considered. We note that the rms energy spread for this BNS configuration is about half of what is expected for autophasing from Figure 8-4.

If the autophasing condition is fulfilled, then we would expect that the betatron oscillations from the initial 1σ beam offset, normalized with the beta function and the beam energy, propagate downstream without perturbations. Figures 5 and 6 show the normalized betatron oscillations and the vertical single bunch emittance growth along the linac. The first figure does not include any initial uncorrelated energy spread, while the second case includes the nominal 1.5% initial energy spread. It is easily seen that the amplitude of the normalized betatron oscillation is not maintained in either case. We note that the initial uncorrelated beam energy spread significantly changes the dynamics in the beginning of the linac. It causes strong filamentation and modifies tolerances for incoming jitter.

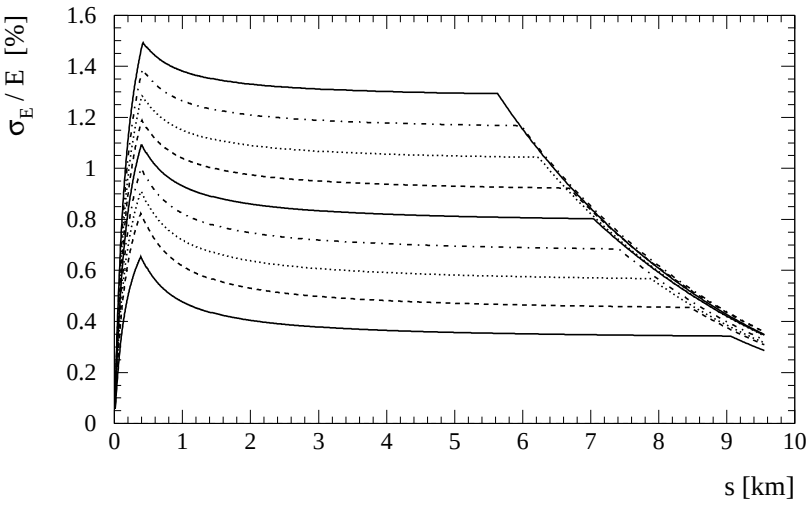

Figure 2: Beam rms energy spread along the linac for different BNS configurations. Note that the initial uncorrelated energy spread was set to zero. The final extracted rms energy spread is fixed to about 0.3% as required by the final focus energy bandwidth. The different BNS configurations are defined in Table 5 and are referred to as number 1 to 9, where 1 is the lowest curve.

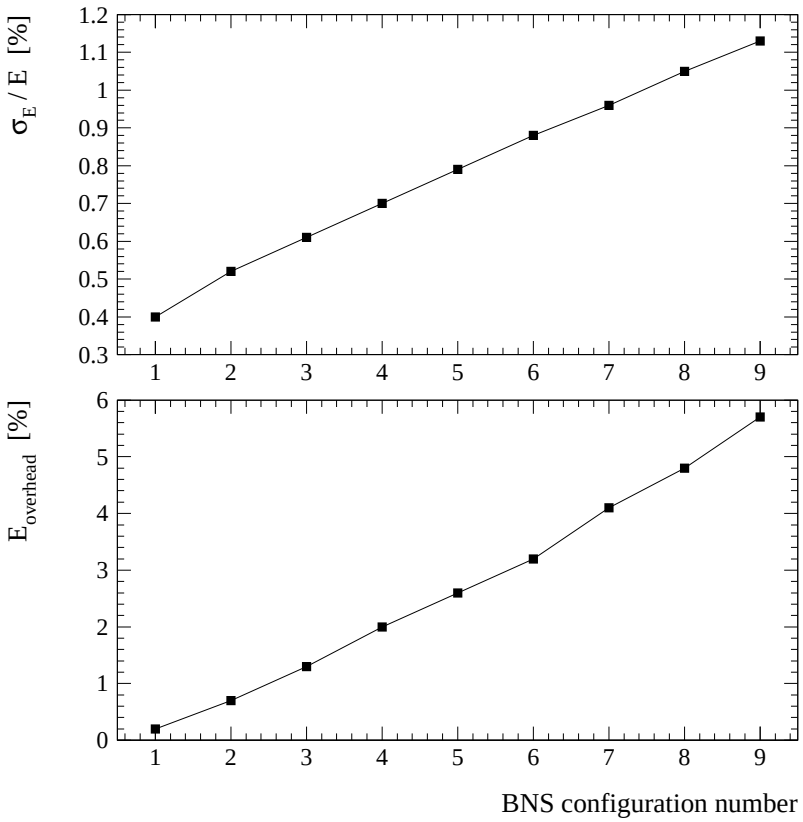

Figure 3: The different BNS configurations from Figure 2 are characterized by the average energy spread σ_E/E along the linac and the BNS energy overhead $E_{overhead}$.

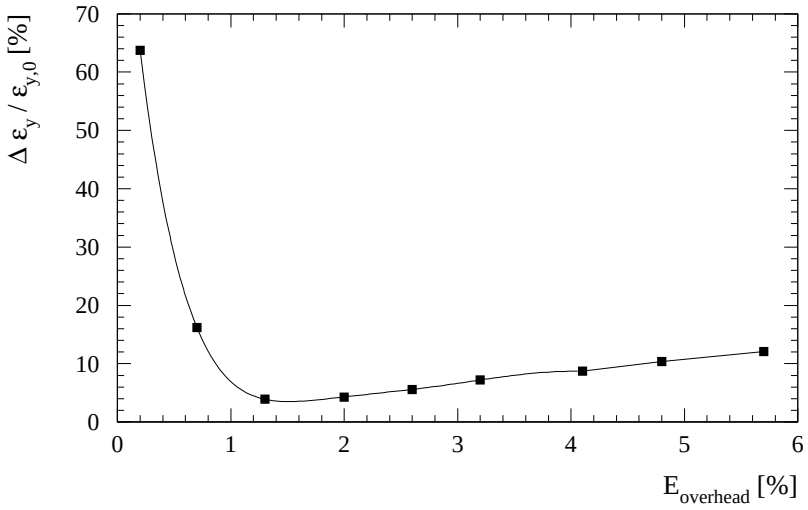

Figure 4: Average vertical emittance growth $\Delta\epsilon_y/\epsilon_{y,0}$ for the different BNS configurations from Figures 2 and 3 and a 1σ (2.2 μm) initial beam offset. The initial uncorrelated beam energy spread is set to zero.

6 Static imperfections and their correction

Imperfections are called static if they do not change during the typical time scale of beam-based alignment and correction procedures. Initially static imperfections in the NLC linacs are allowed to be large compared to the final tolerances. In order to achieve the required tolerances the "conventional" (not beam-based) alignment must be complemented by beam-based alignment techniques. In this section we explain the algorithm proposed for beam-based alignment and its implementation in the simulation program. We discuss detailed simulations that show that the required precision levels can indeed be achieved, even when many additional error sources are included.

6.1 The beam-based alignment algorithm for quadrupoles and RF-structures

The emittance growth is driven by transverse offsets between the beam and the centers of quadrupoles and structures. Those offsets must be effectively minimized in order to maintain the normalized emittances.

The basic concept for the NLC beam-based quadrupole alignment is to use the available BPM information to solve for the beam-to-quadrupole offsets and the initial beam position and angle. Assuming that all beam deflections are caused by the quadrupoles, we can use N BPM measurements to solve for N-2 quadrupole offsets and the initial y, y' of the beam. The positions of the first and last quadrupole in the corrected section are fixed.

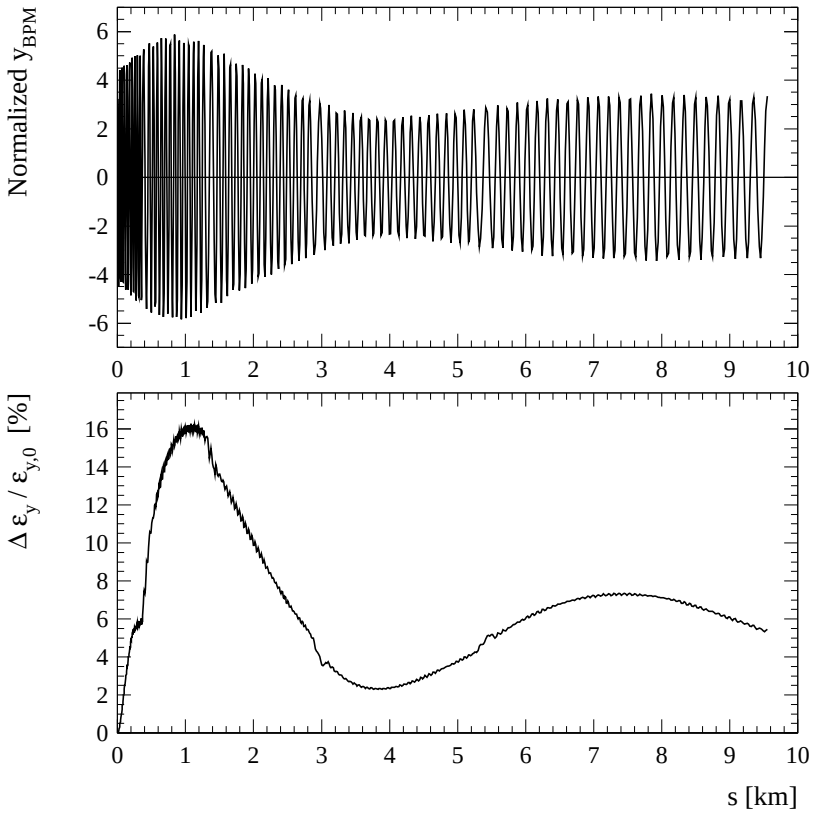

Figure 5: Beam offsets y_{BPM}, normalized with the beta function and the beam energy, and emittance growth $\Delta\epsilon_y/\epsilon_{y,0}$ for a 1σ (2.2 μm) initial beam offset and no initial uncorrelated beam energy spread. The BNS configuration number 3 with a BNS energy overhead of 1.3% is used.

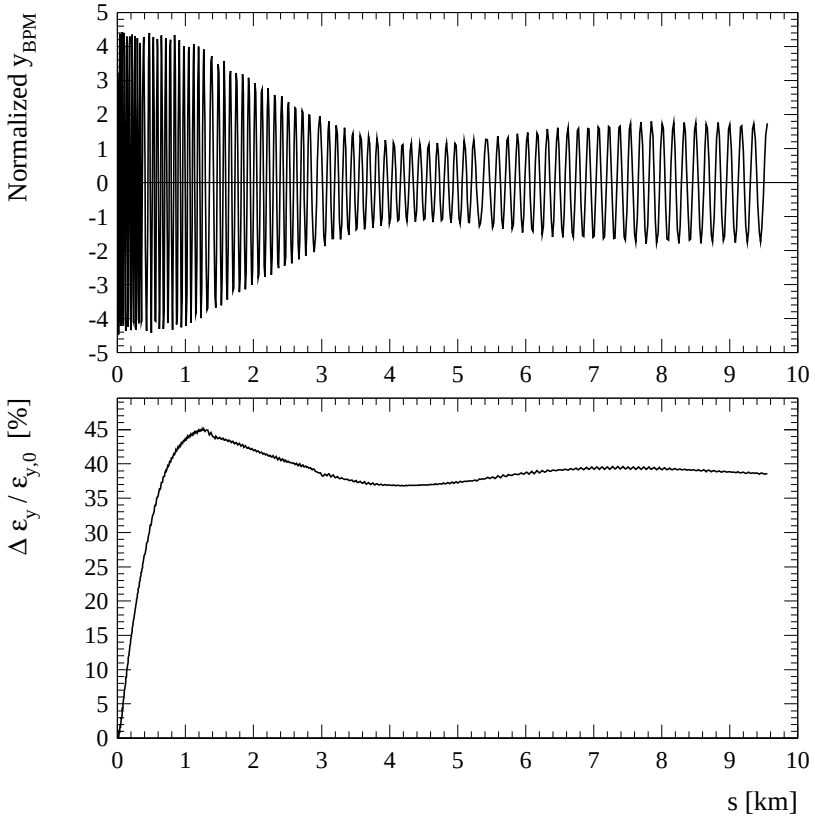

Figure 6: Beam offsets y_{BPM}, normalized with the beta function and the beam energy, and emittance growth $\Delta\epsilon_y/\epsilon_{y,0}$ for a 1σ (2.2 μm) initial beam offset. Here the initial uncorrelated beam energy spread is set to 1.5%. Again we use the BNS configuration number 3 with a BNS energy overhead of 1.3%.

The endpoint BPM's define the reference line for the alignment. If the alignment is done in many sections then the beam is launched from one section into the other with a single dipole corrector at the border between the two. Therefore, for all but the first section we adjust only the initial y'. In the first section we adjust both y and y' of the incoming beam ("launch feedback"). The quadrupoles are aligned with magnet movers at each quadrupole support. Since the optics model is perturbed by wakefields and to account for other imperfections, the alignment is implemented as an iterative process. Furthermore, the quadrupole alignment is interleaved with the alignment of the RF-structures.

The RF accelerator structures have an RF-BPM at each end. Two RF-structures are always mounted on a single support structure. Every support structure can be moved by stepping motors at either end. Thus, for each support structure a total of four RF-BPM's measure the beam positions in the structures and two movers align the girder. The movers are adjusted such that the average RF-BPM reading on a girder is minimized. The RF-structure alignment is performed after each iteration of quadrupole beam-based alignment.

Here, we assume that the step resolution of the magnet and girder movers is infinitely small. The typical step size of 0.25 μm is indeed small compared to the resolution of the RF-BPM's of about 15 μm rms and can therefore be neglected for the RF-structures. However, for quadrupoles the step size of the movers is an important limitation. The problem is avoided by having dipole correctors at each quadrupole that shift its effective magnetic center. Small quadrupole misalignments are therefore "cured" with dipole correctors. If the dipole strengths get large enough they are "exchanged" for a step of the quadrupole mover.

The alignment algorithm that was sketched above was implemented into the simulation program LIAR. First, we consider a simple case where we start with a random quadrupole misalignment of 100 μm rms and assume perfect BPM's and RF-BPM's. Both kinds of BPM's have no offsets and zero resolution. The quadrupole alignment is done in 14 regions to allow for best convergence. Each region contains about 52 quadrupoles and is iterated 15 times. The number of iterations is chosen higher than necessary in order to explore the optimal solution.

The misalignment of quadrupoles, BPM's and RF structures, after the application of the interleaved alignment procedure, is shown in the upper part of Figure 7. The dipole kicks at the bounderies between correction regions are shown in the lower part of the same figure. A very smooth alignment between the endpoints of each section is indeed achieved. At the endpoints the beam is deflected into the next section, causing sharp kinks. The endpoints are not moved and reflect the initial random quadrupole misalignment of 100 μm. Between the endpoints, the alignment is bowed towards zero. The absolute zero line is known to the system only because the initial misalignment was random about it. Constraints on the rms size of magnet movements bias the solution towards the initial average misalignment between endpoints.

The solution shown in Figure 7 is largely determined by the different weights on the "measured" BPM readings, the rms of the calculated magnet movements and the strength of the dipole kick that launches the beam into the alignment section. Changes in

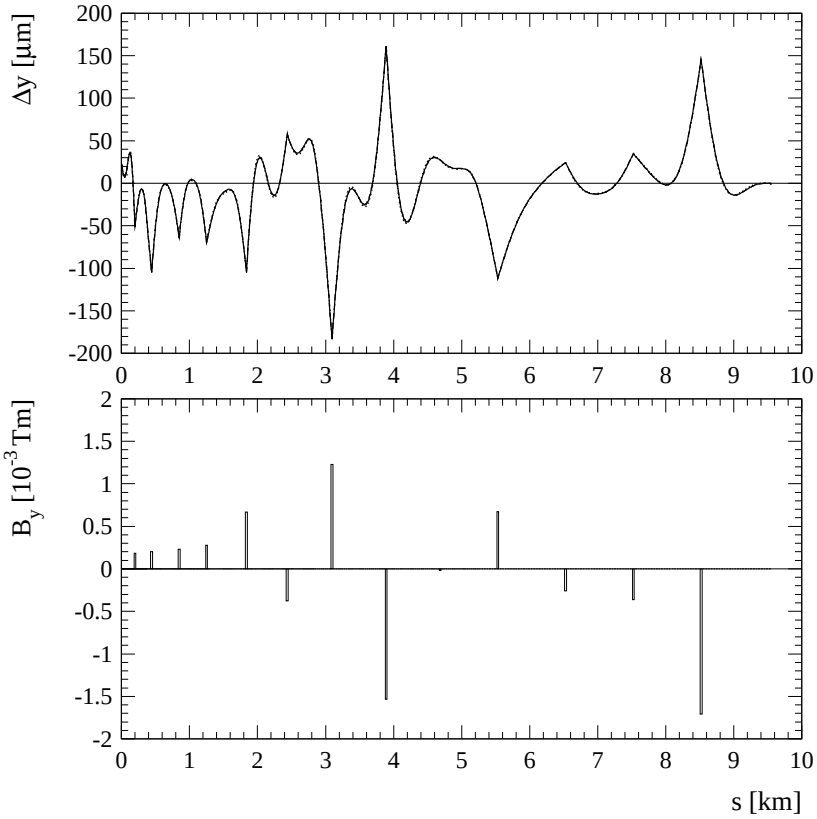

Figure 7: Example of the beam-based alignment algorithm with perfect BPM's and RF-BPM's. The initial random quadrupole misalignment was 100 μm rms. The alignment is done in 14 sections and 15 iterations. At the end of each section a dipole corrector is used to launch the beam into the next section. The upper plot shows the misalignment Δy of quadrupoles, RF-structures and BPM's after alignment. The lower plot shows the integrated fields of the dipole correctors.

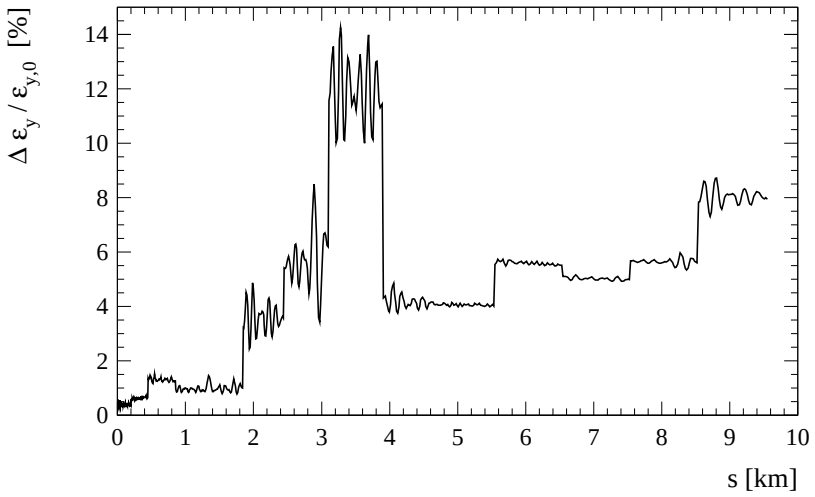

Figure 8: Emittance growth $\Delta\epsilon_y/\epsilon_{y,0}$ along the linac for the example from Figure 7. Note that the steps occur at the end of the alignment sections where dipole kicks launch the beam into the next section.

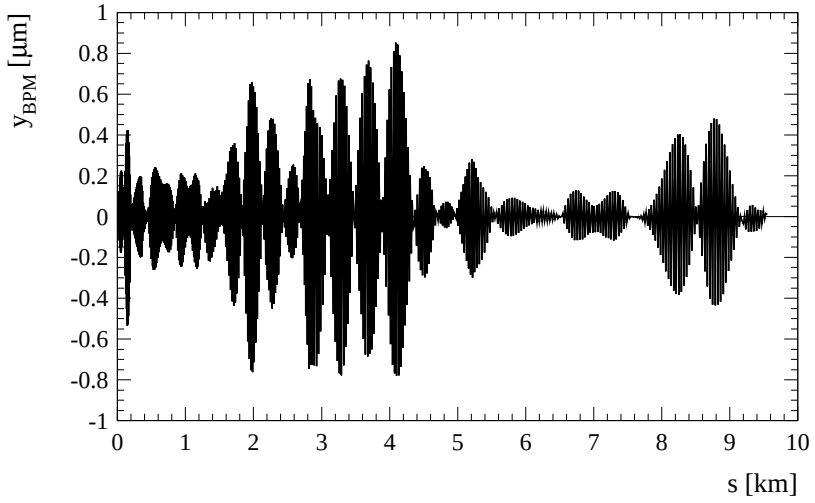

Figure 9: Vertical trajectory offsets at the quadrupole BPM's along the linac for the example from Figure 7. The residual beam offsets in the quadrupoles bend the beam along the bowed alignment path. They are not betatron oscillations and cause only negligible emittance growth (compare to Figure 8).

the relative weights will result in solutions that are not equivilant in terms of emittance growth. We have chosen to constrain the rms magnet movements and the rms of the "measured" BPM readings relatively strongly while allowing for large dipole kicks. This choice of weights results in a small final emittance growth.

The vertical single-bunch emittance growth and the trajectory along the linac are shown in Figures 8 and 9. The trajectory shows residual sub-micron beam offsets in the quadrupoles. The alignment algorithm puts in those offsets in order to bend the beam along the curved alignment path. If the beam had no offsets in the quadrupoles then it would have to go straight. Figure 8 shows that the small beam offsets cause no significant emittance growth. The residual emittance growth occurs mainly at the transitions from one sector to the next. The large dispersive deflections cause a stepwise emittance growth behavior. One can imagine smoothing the transitions by distributing the beam deflection. A better method would be to also move the sector endpoint quadrupoles such that the deflection kicks are minimized.

We should stress that the present algorithm already works very well. The quadrupole and structure alignment is minimized over short wavelengths and beam offsets with respect to the BPM's are effectively reduced from many cm's to the sub-micron level. The smooth alignment of quadrupoles and structures minimizes the vertical emittance growth to about 20%. The convergence of the method is illustrated in Figure 10 where the vertical single-bunch emittance growth and the vertical rms beam offset in the BPM's are shown as a function of iteration number. It is seen that after about 5 iterations a very reasonable situation is achieved with almost no further improvements after about 15 iterations.

The emittance growth for the case of perfect BPM's is a function of the initial quadrupole misalignment which determines the magnitude of the dispersive deflections between sections. This is shown in Figure 11. The vertical single-bunch emittance growth and the rms trajectory offset at the BPM's are shown as a function of the initial rms quadrupole offset. As expected, the rms trajectory offset in Figure 11 increases linearly and the vertical emittance growth increases quadratically with the initial rms quadrupole misalignment.

Now we consider a more realistic case where the BPM's have a 2 μm rms static offset with respect to the quadrupoles and a 1 μm rms resolution. The initial quadrupole misalignment is 50 μm rms. We still assume perfect RF-BPM's. The alignment is done in 14 sections and 5 iterations. Figure 12 shows the average vertical single-bunch emittance growth for the different BNS cases and the imperfections defined above. The BNS configuration number 3 still yields the smallest emittance growth. However, due to the additional BPM imperfections, the emittance growth for the nominal BNS increased from about 7% to about 28%. This is well below the emittance growth budget of 175% for NLC-IIb.

6.2 The effects of transverse long-range wakefields

Thus far, we have only considered single-bunch effects. However, for the bunch train of 90 bunches, transverse long-range wakefields become important. In order to set the scale

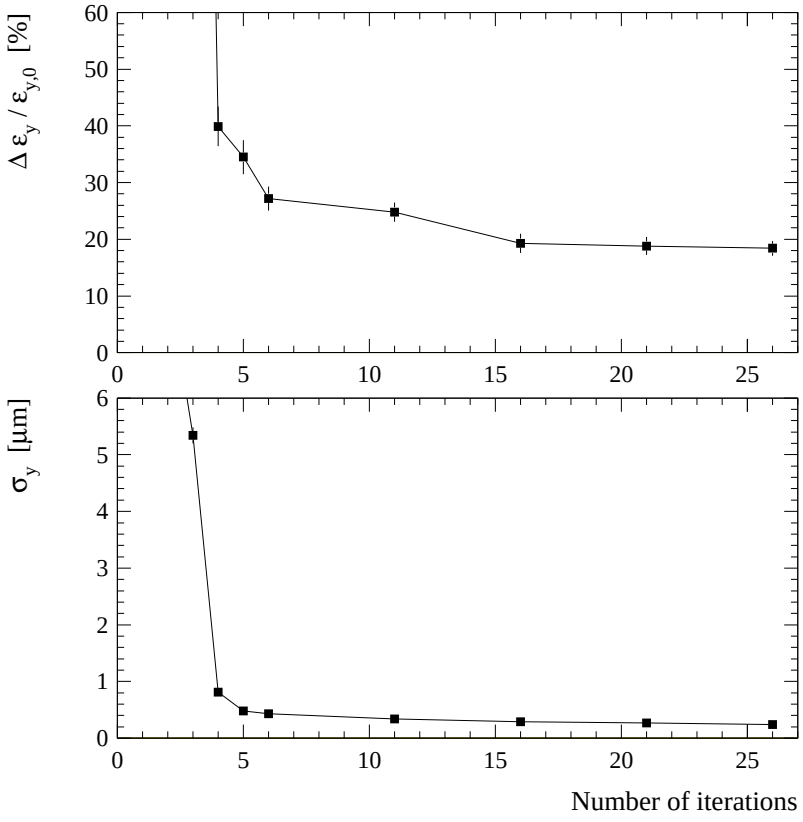

Figure 10: Convergence of the alignment algorithm for an initial random quadrupole misalignment of 100 μm rms and perfect BPM's. The upper plot shows the average emittance growth $\Delta\epsilon_y/\epsilon_{y,0}$ as a function of the iteration number. The lower plot shows the corresponding rms trajectory offset with respect to the BPM's.

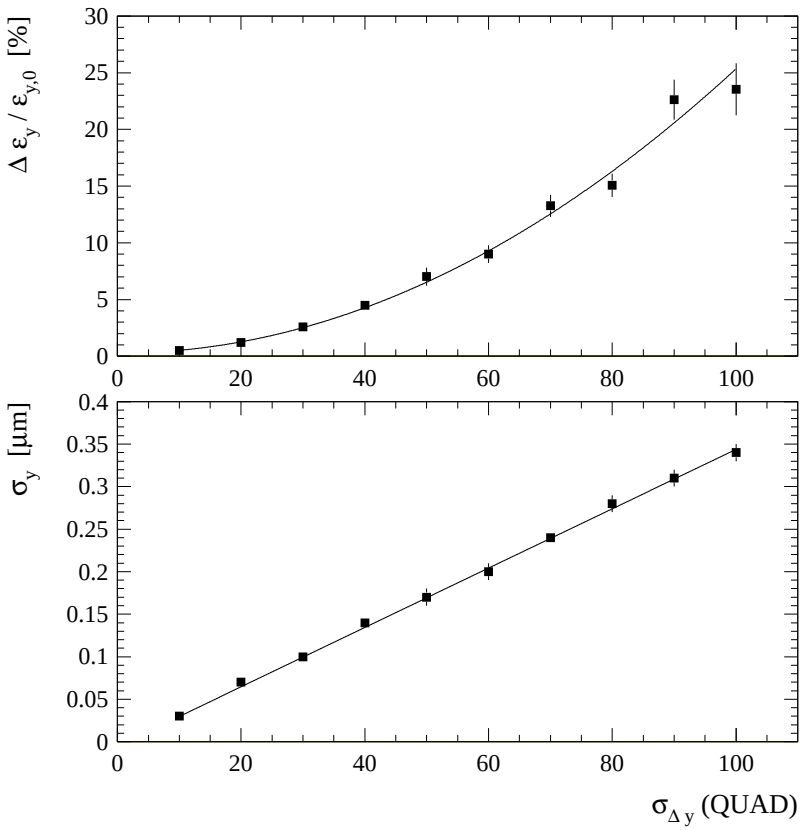

Figure 11: The average emittance growth $\Delta\epsilon_y/\epsilon_{y,0}$ and rms trajectory offset σ_y after alignment versus the initial rms quadrupole misalignment $\sigma_{\Delta y}$.

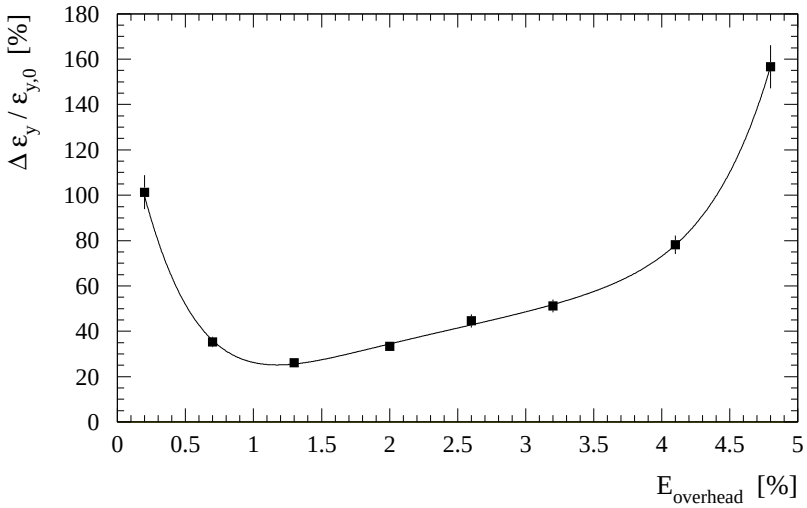

Figure 12: Average emittance growth $\Delta\epsilon_y/\epsilon_{y,0}$ after alignment for different BNS configurations. Here we assume an initial quadrupole alignment of 50 μm rms, a static BPM to quadrupole offset of 2 μm rms, a BPM-resolution of 1 μm rms and perfect RF-BPM's. The alignment is done in 14 sections and 5 iterations.

of those effects, we show the multibunch emittance blowup due to a 1σ initial vertical beam offset. Figure 13 shows the special case where each bunch is described as a single beam ellipse (zero bunch length). Single-bunch wakefields do not apply and the phase space distribution of the bunch train only reflects long-range wakefields. The phase space distribution of the bunches is compared to the beam ellipse that is obtained from the average single-bunch emittance. The bunches spread all over the beam ellipse but do not reach far beyond that. Multibunch emittance growth is therefore limited and is found to be 25.6%.

Figure 14 shows the same case for a more realistic beam distribution. The bunch has a finite length and single bunch wakefields apply. Filamentation and BNS damping cause the phase space distribution of the bunches to be smaller. In this case the emittance of the first bunch grows by 38.7%, the average single bunch emittance growth is 49.0% and the total emittance growth is 54.4%. The difference between the last two numbers reflects the impact of the long-range transverse wakefields. Here emittance growth is dominated by single-bunch wakefield effects.

6.3 Betatron coupling

In the NLC, the horizontal emittance is about 100 times larger than the vertical emittance. Betatron coupling can couple part of the large horizontal emittance into the vertical plane. This effect is illustrated in Figure 15. Since the horizontal trajectory was kept flat for

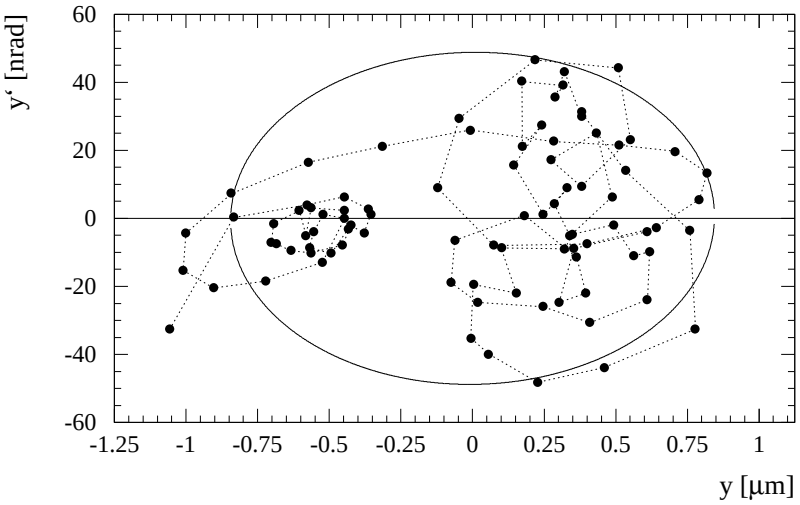

Figure 13: Phase space locations y and y' of the bunches at the end of the linac for a 1σ initial vertical beam offset. y and y' are referenced to their average values. The bunch positions are compared to the beam ellipse from the average single-bunch emittance. Every bunch is tracked as a single beam ellipse so that no single-bunch wakefield effects apply. For this case a multibunch emittance growth of 25.6% was calculated.

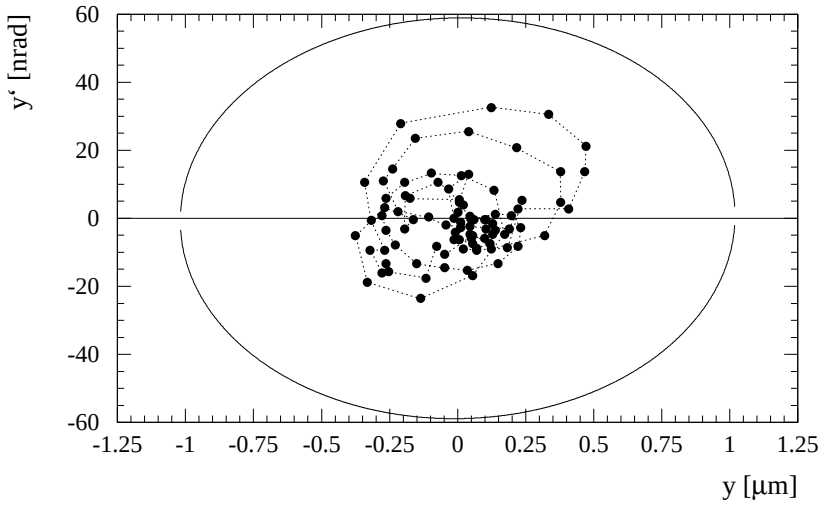

Figure 14: Phase space locations y and y' of the bunches at the end of the linac for a 1σ initial vertical beam offset. y and y' are referenced to their average values. Single-bunch wakefield effects are included. The amplitude of the incoming betatron oscillation and the resulting long-range wakefield effects are reduced by filamentation. The bunch positions are compared to the beam ellipse from the average single-bunch emittance. Here we obtain a total emittance growth of 54.4%. The emittance growth of the first bunch is 38.7% and the average single-bunch emittance growth is 49.0%.

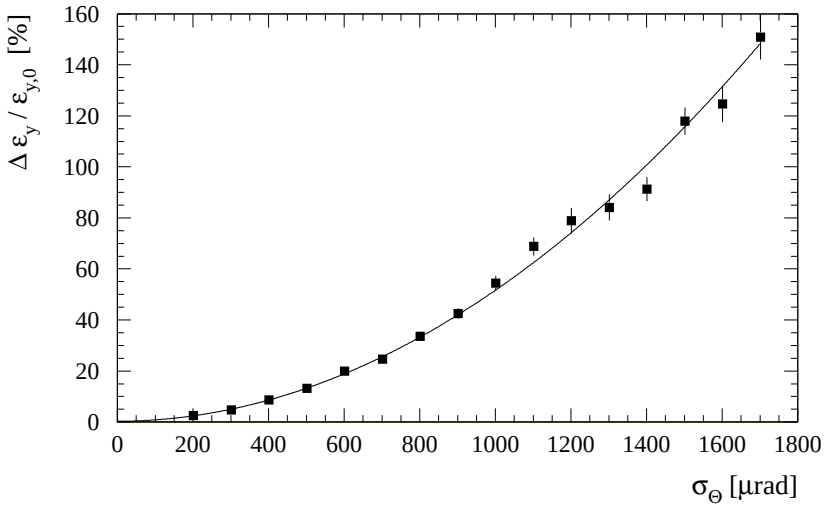

Figure 15: Average vertical emittance growth $\Delta\epsilon_y/\epsilon_{y,0}$ as a function of the rms quadrupole roll θ around the longitudinal direction. There are no horizontal beam offsets in the quadrupoles. The data only shows "emittance coupling".

this study, no vertical betatron oscillations are induced from the coupling. If there were any, they would be absorbed into the alignment and trajectory correction. The emittance growth shows a quadratic dependence on the rms quadrupole roll angle. Assuming the tolerance value of the roll angle of about 300 μrad rms, the emittance growth is well below 10% and is not important.

6.4 Full simulation

For a full simulation, we put the most important imperfections together, apply the correction algorithms and observe the emittance growth. In order to illustrate the importance of the several effects, we proceed in steps. For each case we quote the emittance growth $\Delta\epsilon_y/\epsilon_{y,0}$ at the end of the linac and the rms beam offset σ_y at the BPM's.

1. Initial random quadrupole misalignment of 100 μm rms. RF structures are aligned to the beam.
$$\frac{\Delta\epsilon_y}{\epsilon_{y,0}} = (24.4 \pm 2.3)\%$$
$$\sigma_y = (0.35 \pm 0.01)\mu m$$

2. Add: BPM resolution of 1 μm rms. Static BPM-to-quadrupole offsets of 2 μm rms.
$$\frac{\Delta\epsilon_y}{\epsilon_{y,0}} = (41.1 \pm 2.4)\%$$

$$\sigma_y = (1.08 \pm 0.01)\mu m$$

3. Add: RF-BPM resolution of 15 μm rms.

$$\frac{\Delta\epsilon_y}{\epsilon_{y,0}} = (90.2 \pm 6.0)\%$$

$$\sigma_y = (1.21 \pm 0.01)\mu m$$

4. Add: Rf-phase errors of 1° rms. RF amplitude errors of 0.2% rms. Quadrupole roll errors of 300 μrad rms. Quadrupole gradient errors of 0.3% rms.

$$\frac{\Delta\epsilon_y}{\epsilon_{y,0}} = (97.8 \pm 3.6)\%$$

$$\sigma_y = (1.22 \pm 0.01)\mu m$$

5. Add: Multibunch long-range wakefield effects.

$$\frac{\Delta\epsilon_y}{\epsilon_{y,0}} = (106.6 \pm 3.9)\%$$

$$\sigma_y = (1.23 \pm 0.01)\mu m$$

All emittance growth numbers, apart from the last one, refer to the single-bunch emittance growth. The total multibunch emittance growth of about 110% is well below the allowed emittance dilution of 175% for NLC-IIb (compare Table 8-2). Internal structure misalignments, special multibunch imperfections and the effects of missing BPM's will be added to the simulations in future studies.

The most important imperfections considered so far are BPM and RF-BPM errors. They determine the quality of the correction and the residual emittance growth. In all cases, the correction and alignment is done on the first bunch, assuming that all other bunches behave similarly. The small additional multibunch emittance growth shows that this is a valid assumption, although we have not yet included the effects of internal structure misalignments. The distribution of emittance growth for different error distributions is shown in Figure 16 for the full simulation (last case). The exponential tail for large emittance dilutions tends to bias the average emittance growth towards larger values. It results from error distributions that have a large component at the betatron frequency. Fortunately, these errors are easily corrected using bump (global) correction methods.

Figure 17 shows an alternate way to quantify the effect of imperfections. The so-called "luminosity reduction" (L_y) is calculated from a cross-correlation of the bunch distributions with themselves. Beam tails are naturally de-weighted in this process. The result is quoted as the fraction of the maximum luminosity that would be achieved for the particular case. The luminosity reduction comes out to be 71.1% for the full NLC simulation. That means that on average about 70% of the maximum luminosity would be obtained with the given errors.

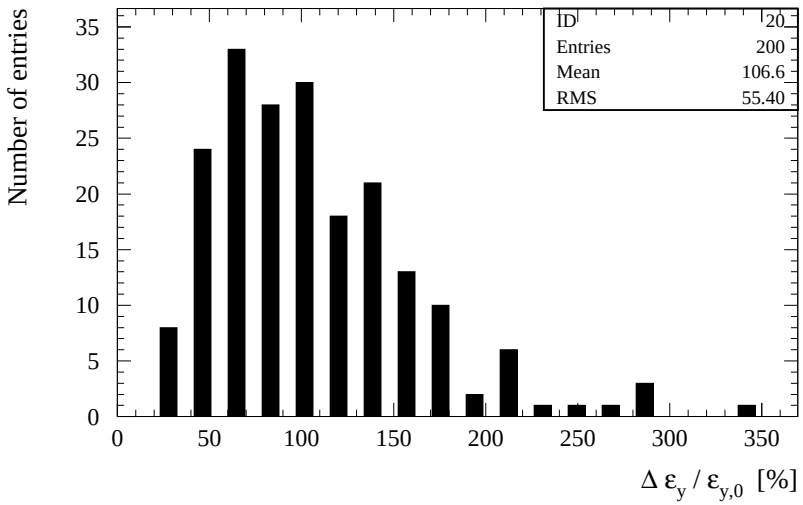

Figure 16: Histogram of vertical emittance growth $\Delta\epsilon_y/\epsilon_{y,0}$ for 200 different error distributions. The average emittance growth is 106.6% ± 3.9%. Note the exponential distribution for large emittance dilutions.

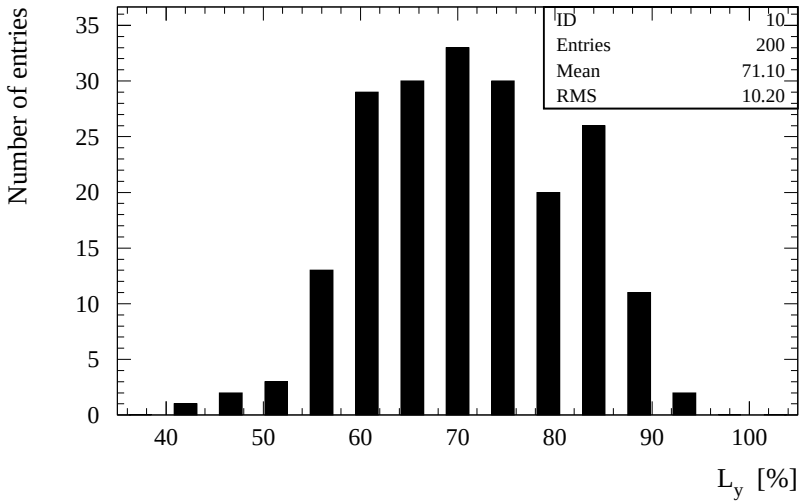

Figure 17: Histogram of the luminosity reduction L_y for 200 different error distributions. The average luminosity factor is 71.1% ± 0.7%.

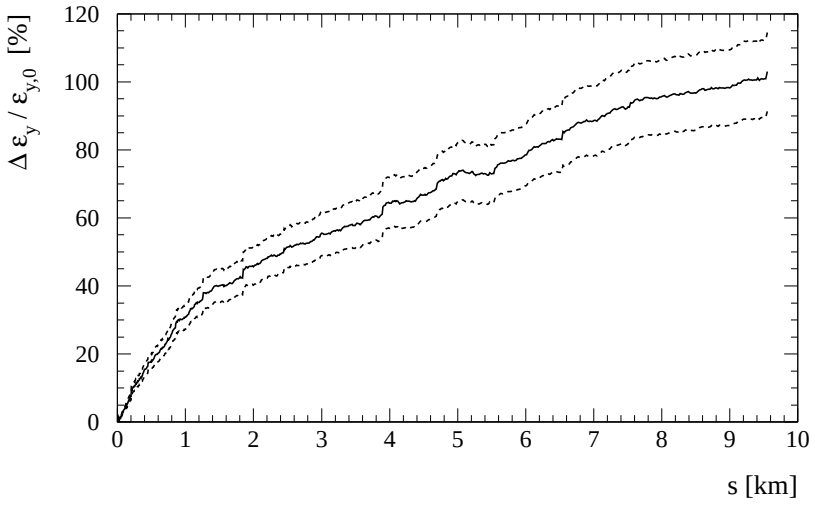

Figure 18: Average emittance growth $\Delta\epsilon_y/\epsilon_{y,0}$ along the linac for the full simulation. The dashed curves specify the errorbands around the average (solid curve).

Figure 18 shows the average emittance growth along the linac for 100 seeds of the full simulation. The growth shows a square-root dependence on the longitudinal position s. No particularly bad region can be identified and the emittance growth behaves rather smoothly. Small residual step increases of the emittance can be seen. They are caused by the transitions between alignment sections. However, they are of little importance to the overall emittance growth.

Figures 19, 20 and 21 show an example of the long-range wakefield effects for the full set of imperfections. Figure 21 is of particular interest. The single-bunch emittance is shown as a function of the bunch number. It shows an oscillatory behavior and is even reduced below the value of the first bunch for some of the trailing bunches. Long-range wakefields induce bunch oscillations that can work as "emittance bumps" and reduce emittance. If one could measure the emittances and trajectories of all bunches one could pick the bunch with the smallest emittance and use multibunch kickers to correct the other bunches to this reference. The multibunch scheme can in principal be used to conveniently explore the phase space to find the smallest possible emittance dilution.

7 Stability

Stability questions determine how often the alignment and correction algorithms need to be applied. In the previous section we described a procedure that serves as both the alignment and trajectory correction algorithm. We have shown that static imperfections can be corrected down to the required levels. Now we consider the question of how stable

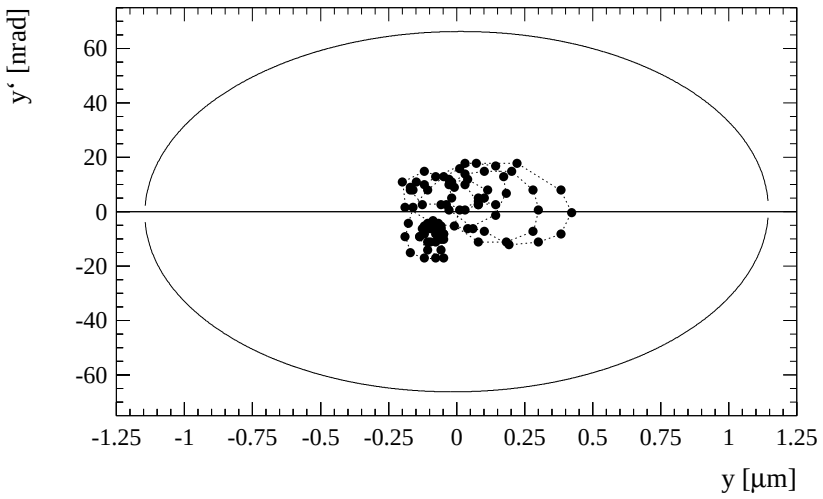

Figure 19: Example of the vertical phase space distribution of the bunch train at the end of the linac. The bunch locations are compared to the beam ellipse as obtained from the average single-bunch emittance. The total vertical emittance growth is 89.0% for this case. This is to be compared to an emittance growth of the first bunch of 83.0%, and an average single-bunch emittance growth of 85.2%.

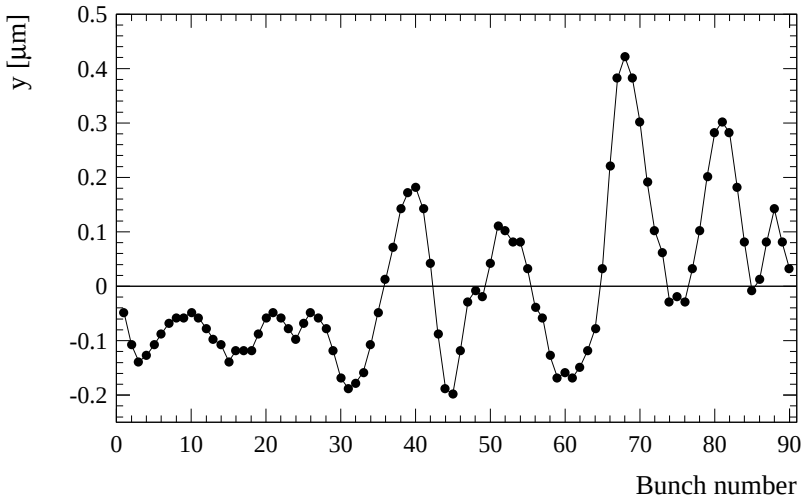

Figure 20: Vertical bunch positions y as a function of bunch number at the end of the linac (same example as in Figure 19).

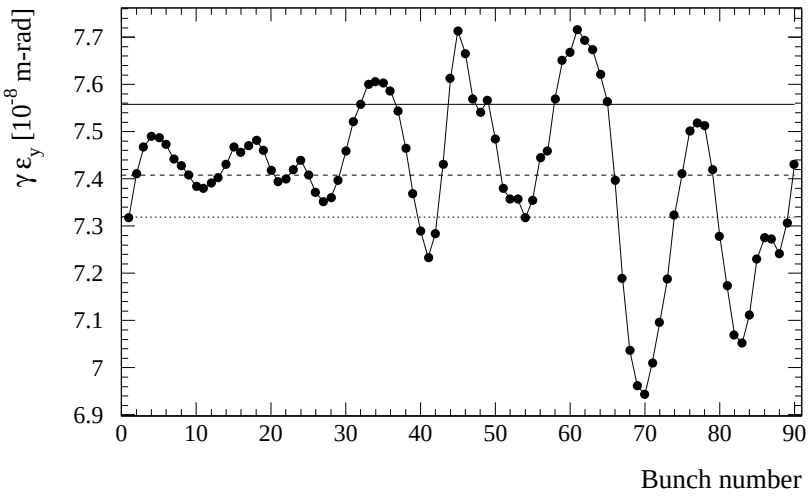

Figure 21: Vertical normalized single-bunch emittance ϵ_y as a function of bunch number at the end of the linac (same example as in Figures 19 and 20). The three lines indicate the emittance growth of the first bunch (dotted), the average single-bunch emittance growth (dashed) and the total beam emittance growth (solid).

the optimized linac is and how fast it deteriorates. From the beam dynamics point of view, linac stability problems are dominated by quadrupole drifts; the quadrupoles generally have the tightest alignment tolerances.

Here we do not discuss BPM stability questions in detail. However, the requirements are tight. For the alignment algorithm we require a 2 μm static rms offset between the BPM and quadrupole centers. This tolerance can be achieved with a time consuming beam-based alignment procedure and it must be stable over signifcant periods of times (days). The question of BPM stability is discussed elsewhere. Since quadrupoles and BPM's are mechanically mounted together the BPM stability that can be achieved is mainly determined by the BPM electronics, cable lengths and similar factors.

7.1 Quadrupole vibrations

Vibrations are fast random motions of the quadrupole alignment around its average position. Here we assume that the vibrations are white noise and that they are not damped by trajectory feedbacks. In reality the quadrupole vibrations due to ground motion, cooling water turbulence, etc will depend on frequency and will be partly suppressed by the trajectory feedbacks.

The average vertical emittance growth is shown in Figure 22 as a function of the vertical rms quadrupole offset $\sigma_{\Delta y}$. Here we only consider single-bunch emittance growth with respect to the beam centroid. Offsets that make the beams miss at the IP are

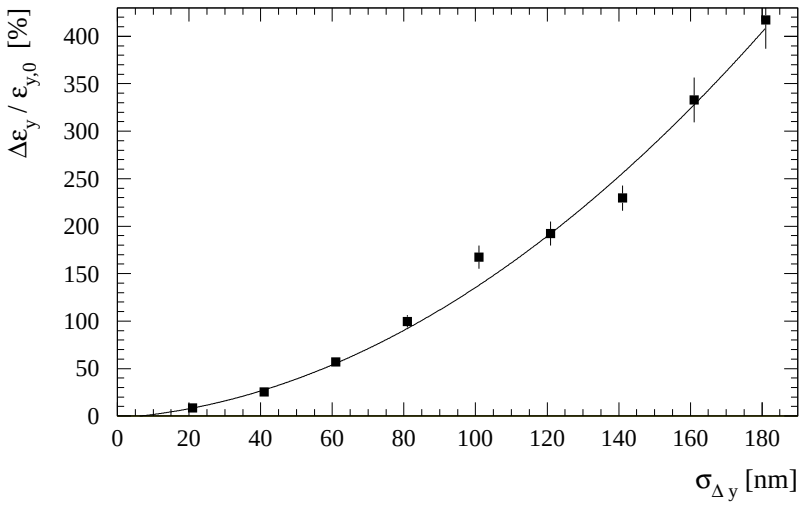

Figure 22: Average single-bunch emittance growth $\Delta\epsilon_y/\epsilon_{y,0}$ as a function of the rms quadrupole offset Δy.

assumed to be suppressed fast feedbacks. Those effects are discussed in more detail in Section 8.3 and in the final focus chapter. From Figure 22 we see that the quadrupole white noise jitter should be kept below 20 nm in order to avoid single-bunch emittance growth in excess of 10%; this tolerance is well above the measured quadrupole jitter. Note that a tighter tolerance results if one considers the the emittance growth with respect to the beam axis.

The emittance growth for quadrupole jitter is mainly caused by the uncorrected betatron oscillation that builds up along the linac. This will be discussed in the next section.

7.2 ATL-like alignment drifts

Next, we consider the question of how often the alignment and correction algorithm needs to be applied. Assuming a perfect starting point (flat trajectory, no emittance growth) we let the alignment drift and observe the deterioration of the trajectory and the emittance. In order to model alignment drifts we use the ATL-model. The ATL-model predicts that the rms vertical misalignment $\sigma_{\Delta y}$ (in μm) deteriorates with time T (in seconds) and over the length L (in m) as follows:

$$\sigma_{\Delta y}^2 = A \cdot T \cdot L$$

We use an A coefficient of $5 \times 10^{-7} \mu\text{m}^2/\text{s/m}$. This value was inferred from data taken on the SLAC site for times T over 30 hours. We should caution that the validity of the ATL-model (diffusive drifts) is not well established. Recent observations indicate a linear increase of the rms misalignment with time for longer periods (systematic drifts).

Assuming diffusive alignment drifts from the ATL-model for time periods of the order of hours might well be overly pessimistic.

Figure 23 illustrates ATL-like alignment drifts. It shows the displacements and corresponding trajectory offsets at the BPM's after 30 minutes of deterioration. The offsets of quadrupoles, BPM's and RF-structures are overlaid in the plot and are essentially indistinguishable. The trajectory offsets at the BPM's show the coherent betatron oscillations that build up. The dotted lines indicate the locations of seven trajectory feedbacks that constrain y and y' to zero. The coherent betatron oscillations are thus broken up into eight smaller oscillations. The oscillation amplitude is a few μm and is large enough to be detected with a BPM resolution of 1 μm.

A histogram of the vertical single-bunch emittance growth from alignment drifts after 30 minutes and an A of 5×10^{-7} μm^2/s/m is shown in Figure 24. The average emittance growth is found to be $29.0\% \pm 0.8\%$. This size of emittance growth will prompt a beam-based alignment of the quadrupoles, that serves as an effective trajectory correction at the same time. Note, however, the exponential distribution for large emittance dilutions. The most probable emittance growth is only about 10%. Figure 25 shows a histogram for the luminosity reduction in the same case. The distribution shows an approximately Gaussian distribution for smaller luminosity, with an average luminosity of about 90% of its ideal value.

The average emittance growth along the linac is shown in Figure 26. The locations of the trajectory feedbacks are clearly seen. As a coherent betatron oscillation builds up the emittance starts to grow exponentially. The feedbacks stop this exponential growth. More effective feedbacks can be imagined if the average y and y' is minimized up to the next feedback instead of correcting y and y' locally.

Figure 27 shows the average vertical single-bunch emittance growth for different BNS configurations. We consider the same case as above. All previous results were obtained using the standard BNS configuration with an energy overhead of 1.3%. Figure 27 shows that BNS configurations with higher energy overheads reduce the emittance growth from 29% to about 16%. This result is in better agreement with the simple two-particle model autophase condition than the other results that were discussed before. One can therefore imagine to trade alignment performance against better stability. However, this is not necessary.

Let us relate the ATL-like alignment drifts to the other results. Since the emittance growth is linear in time we would get an additional average emittance growth of about 15% when we assume a beam-based alignment every 30 minutes. This is about a factor of six smaller than the emittance growth expected after beam-based alignment of quadrupoles and RF-structures. It is small enough not to be an important limitation of the NLC linac performance as long as the linacs are corrected regularly every 30 minutes. Since the alignment and correction algorithm does not interfere with the standard operation, its frequent application should be no major obstacle.

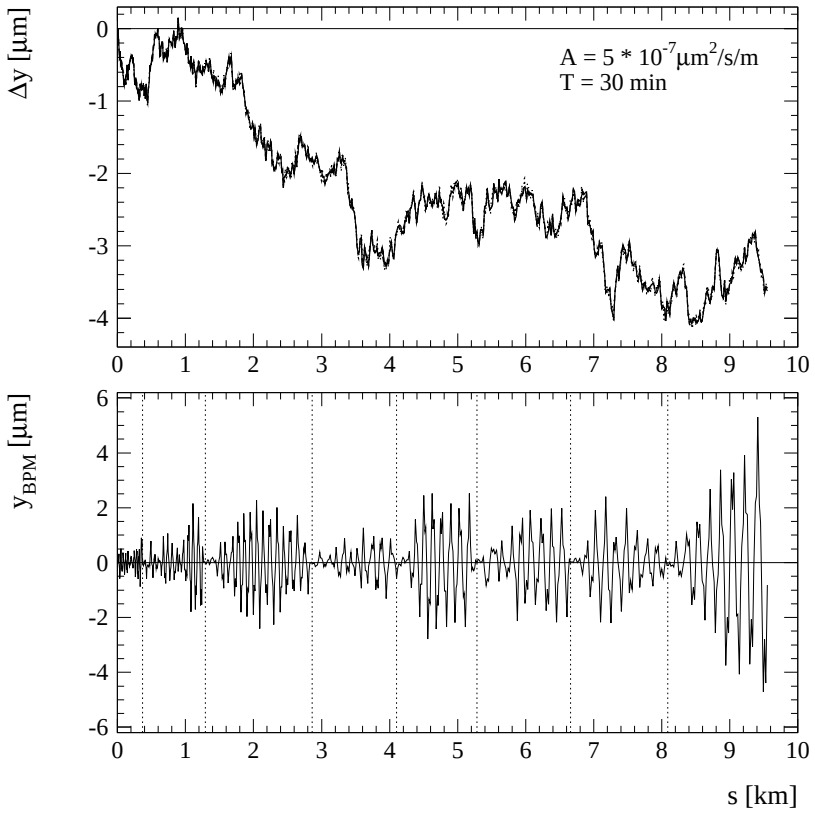

Figure 23: Example of ATL-like alignment drifts. The upper plot shows the displacements of quadrupoles, RF-structures and BPM's after 30 minutes with an A-coefficient of 5×10^{-7} μm^2/s/m. The alignment was flat initially. The lower plot shows the corresponding trajectory offsets y_{BPM} at the BPM's. The dotted lines indicate the locations of trajectory feedbacks where y and y' are corrected back to zero. Thus the size of coherent betatron oscillations is constrained.

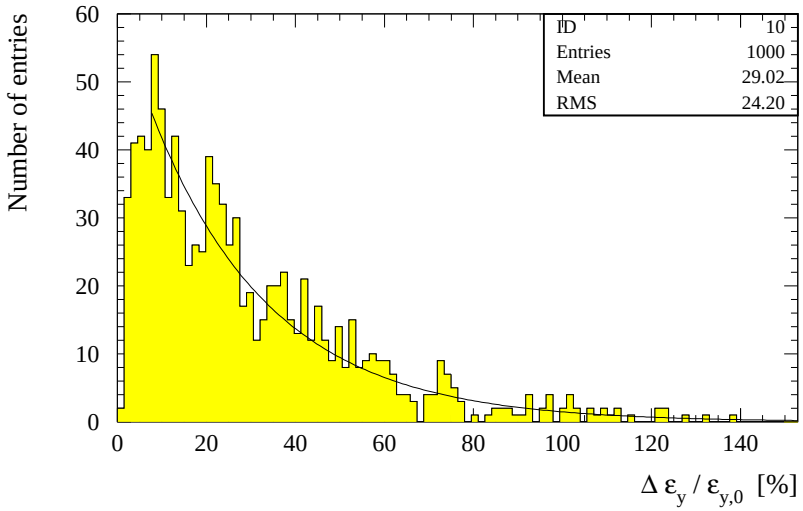

Figure 24: Histogram of vertical emittance growth $\Delta\epsilon_y/\epsilon_{y,0}$ for 1000 different error distributions. The average emittance growth is 29.0% ± 0.8%. The solid curve shows an exponential fit for large emittance dilutions.

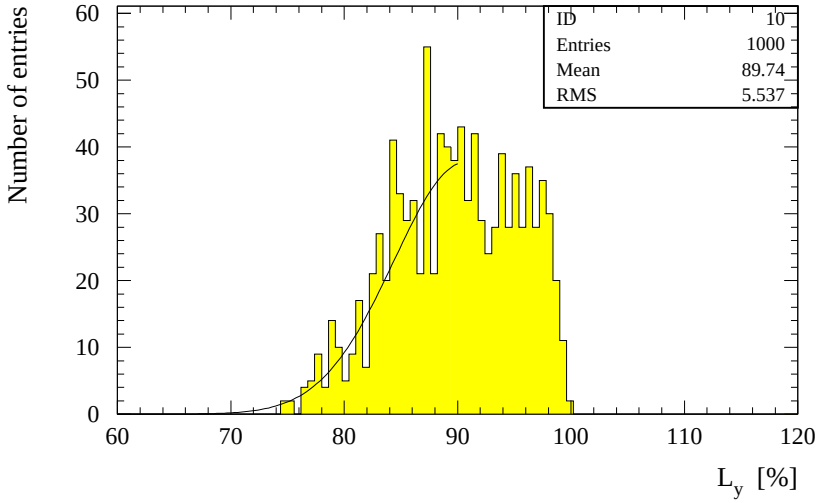

Figure 25: Histogram of the luminosity factor L_y for 1000 different error distributions. The average luminosity is 89.7% ± 0.2%. The solid curve shows a Gaussian fit to the lower half of the distribution.

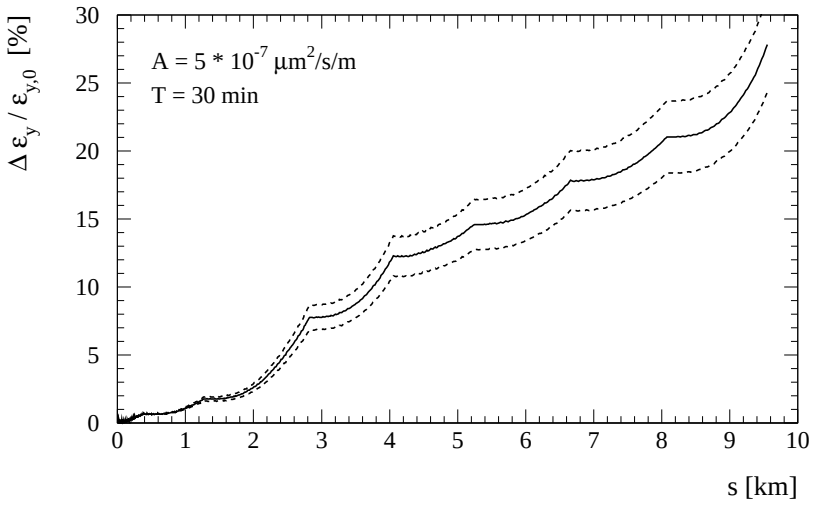

Figure 26: Average vertical emittance growth $\Delta\epsilon_y/\epsilon_{y,0}$ along the linac for ATL-like drifts after 30 minutes. We assume an A-coefficient of 5×10^{-7} μm^2/s/m. The dashed curves specify the errorbands around the average (solid curve).

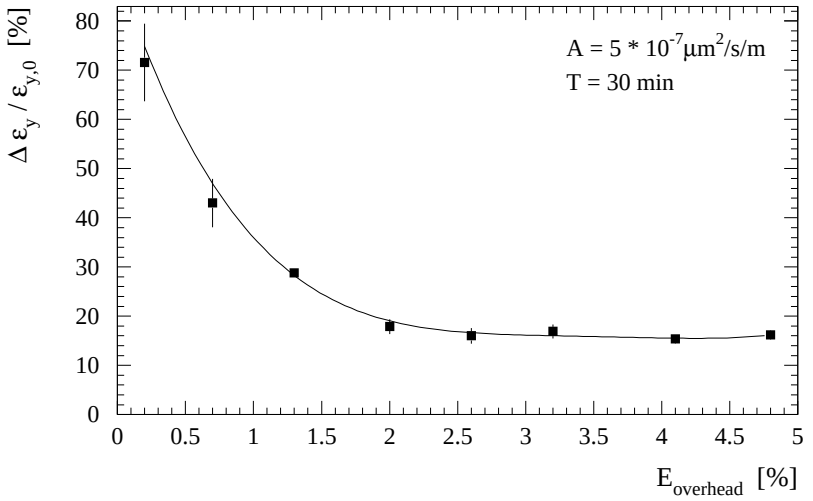

Figure 27: Average vertical emittance growth $\Delta\epsilon_y/\epsilon_{y,0}$ from ATL-like alignment drifts for different BNS configurations.

8 Summary and outlook

A beam-based alignment algorithm for quadrupoles and RF-structures was simulated with a realistic BNS configuration. It was shown that the large initial misalignments from conventional alignment procedures can be corrected to acceptable levels. The emittance growth that finally can be achieved depends on the initial misalignment and most importantly on the performance of the BPM's and RF-BPM's. Assuming an initial misalignment of 100 μm rms, static BPM to quadrupole offsets of 2 μm rms, a BPM resolution of 1 μm rms and an RF-BPM resolution of 15 μm rms, we find an average emittance growth of 90.2% $\pm$ 6.0% for a single bunch. Adding errors of the RF-phases, RF-amplitudes, quadrupole roll angles and quadrupole gradient errors increases the emittance growth to 97.8% $\pm$ 3.6%. Adding the effects of transverse long-range wakefields on the bunch train yields the final multibunch emittance growth of 106.6% $\pm$ 3.9%. This emittance growth is smaller than the allowed total emittance growth of 175%. As the emittances roughly add in quadrature the impact of additional imperfections gets smaller with larger emittances. It is anticipated that the alignment algorithm can be further optimized by smoothing the transitions between alignment sections. Further details can be found in the text.

The dominant stability problem is caused by drifts of the quadrupole alignment. We simulated this effect by using the ATL-model with a coefficient $A = 5 \times 10^{-7} \mu\text{m}^2/\text{s/m}$ as measured at SLAC. The use of this model for times of about 1 hour might be overly pessimistic. We showed that the alignment drifts drive coherent betatron oscillations that lead to exponential emittance growth. The addition of seven trajectory feedbacks breaks the coherent betatron oscillation down into eight smaller oscillations. Assuming a beam-based quadrupole alignment every 30 minutes, we get an additional average emittance growth contribution of 15%. Since the emittances roughly add up in quadrature, this is small compared to the 107% average emittance growth after alignment. The alignment algorithm does not interfere with the normal linac operations, so that it can be applied very frequently. We conclude that we can handle alignment drifts safely.

Future simulation studies will include internal structure misalignments, multibunch imperfections (bunch-to-bunch charge, energy, etc. variations) and the effects of missing BPM's. In addition, we further want to apply emittance bumps in order to compensate the emittance growth below what has already been achieved. Finally, we need to study the impact of different bunch shapes on the linac emittance transport and we need to simulate the collimation requirements at the end of the linacs.

References

[1] The NLC Design Group, "Zeroth-Order Design Report for the Next Linear Collider", SLAC report 474 (1996).